WILEY

The Institution of Engineering and Technology

ORIGINAL RESEARCH OPEN ACCESS

An Entropy-Based Hybrid Conjugate Gradient Scheme for Locating High Impedance Faults in DC Microgrids

Reza Rahmani | Seyed Hossein Hesamedin Sadeghi | Hossein Askarian Abyaneh | Mohammad Javad Emadi

Department of Electrical Engineering, Amirkabir University of Technology (Tehran PolyTechnic), Teharn, Iran

Correspondence: Seyed Hossein Hesamedin Sadeghi (sadeghi@aut.ac.ir)

Received: 30 December 2024 | **Revised:** 8 April 2025 | **Accepted:** 17 April 2025

Handling Editor: Yi Wang

Funding: The authors received no specific funding for this work.

Keywords: fault location | microgrid design | optimisation

ABSTRACT

This Paper proposes an efficient inversion scheme based on Shannon entropy to determine the location of high impedance faults (HIFs) in DC microgrids in the presence of noise. The proposed scheme adopts a phenomenological approach that uses a physical model to iteratively solve the inverse problem. The problem is posed as an optimisation problem that determines the most likely location of a fault by minimising an appropriate objective function; it denotes the disparity between the entropy of the current waveforms observed by the protection relays at the time of fault detection and their model-predicted counterparts. A hybrid optimisation technique based on the conjugate gradient method is adopted in the inversion process that secures a robust and fast convergence of the proposed method. The primary advantage of this scheme is its accuracy in noisy environments with no limitation on the type of fault and value of fault impedance. To examine the performance of the proposed scheme, a mesh-type DC microgrid is simulated and the results are compared with one of the state of-the-art methods. It has been shown that the proposed method can accurately locate HIFs with fault resistance as high as 100 Ω and signal-to-noise ratio as low as 20 dB.

1 | Introduction

DC microgrids experience rapid fault currents that need to be interrupted quickly to prevent damage to equipment and ensure safety [1]. By quickly identifying the fault location, repair crews can be dispatched precisely, reducing downtime and restoring power more efficiently.

Apart from the primitive visual approach, the fault location schemes can be divided into two categories, namely, active and passive methods. In an active scheme, the location of the fault can be determined by first injecting proper current or voltage signals into the faulty line using an RLC circuitry, known as probe power unit (PPU) [2]. Analysis of the reflected signals from the fault location is then conducted to pinpoint the fault. In Aluri and Samantaray [3], a portable PPU with a combination of time-domain and frequency-domain analysis is utilised for fault location. This approach employed fast Fourier transform (FFT) and least-square curve fitting to determine the natural oscillating frequency of the fault path. The main advantage of this method is its accuracy; however, it is time-consuming and requires extra equipment that results in a relatively high cost.

In a passive scheme, the voltage and current waveforms captured by the protective relays are utilised to locate a fault. In this context, various methods were devised including the travelling wave method, capacitor source method and artificial intelligence-based method. The travelling wave method relies on measuring the time at which travelling waves reach the endpoints of the faulty line [4–6]. It suffers from a number of issues such as high sampling frequency, complex structure and interference signal. Besides, the difficulty in accurate determination of the arrival time makes this method impractical for short lines (which are often the case in microgrids), or in the case of a fault occurring near the protective relays [7]. Alternatively, in the capacitor source method [8, 9], the governing circuit differential equations are used to relate the current and voltage variations at two ends of the faulty line to the fault location. It is shown that in the event of a fault, the existing capacitors positioned at each end of the line are discharged, resulting in a large fault current. Therefore, the use of the analytical model along with local measurements can ascertain the fault location. The early version of this method requires the synchronised data collected from both sides of the protection zone when the faulty line is fed from both directions. This problem is addressed in Meghwani et al. [10] by formulating an appropriate mathematical model for the faulty line, where the values of the capacitors connected at both sides of the faulty line are to be known as a prior assumption.

Recently, artificial intelligence-based methods have gained momentum. In these methods, an appropriate learning-based process is used to extract the characteristics of the transient state exhibited by voltage and/or current waveforms during a fault and relate them to the location of the fault. For example, the authors in Refs. [11–16] used an artificial neural network and wavelet transform to locate various fault types. Although they can pinpoint faults with high speed and precision, their performance can vary across different networks. This challenge is further amplified by the unpredictable nature of photovoltaic and wind power outputs during weather fluctuations as well as the uncertainty in the microgrid structure and operational mode [17]. To address this, the ensemble classifier method was suggested [18]. This approach anticipates all potential scenarios the microgrid might encounter and devises a unique fault detection and isolation strategy for each situation. However, its real-world applicability has been questioned because of the substantial memory needed to fully capture a microgrid dynamic behaviour [19].

In low-voltage systems, such as DC microgrids, high impedance faults (HIFs) are more likely to occur, causing relatively small fault currents. As a result, the detection and location of this type of fault can be challenging. Additionally, the accuracy of most fault location methods is highly dependent on the value of fault resistance which may undermine their accuracy [20]. Locating HIFs was addressed in several cases in the literature. For example, the authors in Bayati et al. [21] adopted a parameter estimation approach and utilised the sampled values of current for determining fault location. It is shown that the proposed method can locate faults with resistance up to 6 Ω. In Kong and Nian [22], the authors used the Pearson correlation coefficient for fault detection and location that showed accurate performance in the event of a fault, having resistance up to 10 Ω. In Ibrahim et al. [23], a machine-learning-based fault location method was proposed, utilising support vector machines (SVM) and bagged trees to detect, classify and locate faults. The method achieved high accuracy with a maximum fault resistance of 200 Ω. In Mahtani et al. [24] a new method based on controlled re-energizations was proposed. In this method a switched grounding resistor (SGR) and a current-limiting reactor (CLR) was used to analyse the discharge curves and estimate fault location and resistance. The maximum fault resistance of 50 Ω is considered in this method. However, none of these methods has considered the effect of noise that can affect their ability to locate a fault. Alternatively, the authors in Bayati et al. [20] have proposed a support vector machine for determining the location of a HIF. The proposed method considered the effect of noise and was able to detect and locate faults with resistance up to 20 Ω. Also, another method based on least squares support vector machine regression was proposed in Shuai et al. [25] that could detect HIF up to 100 Ω. However, like other machine learning-based methods, this method has its own set of challenges including insufficient quantity of training data, non-representative training data, poor-quality data, overfitting/underfitting the training data etc. In another method, a time domain algorithm for fault location in radial medium voltage DC microgrid is proposed in Nougain et al. [26]. The method is used time-domain analysis and terminal voltage, current and CLR measurements to estimate fault location accurately. By analysing the difference in voltage across the CLR and using current measurements, the algorithm eliminated fault resistance dependency and was robust for fault resistance up to 200 Ω. However, the need for CLR at both ends of each line and a rolling mean filter for noise, increased its cost.

To overcome the HIF and noise issues mentioned above, this paper proposes a phenomenological inversion method to determine the location of a fault in a protected line immediately after being detected by the respective protection relays. The proposed method leverages the concept of current waveform entropy, introduced in Rahmani et al. [27], to extract the average information value associated with fault currents. In Rahmani et al. [27], relative waveform entropy was employed for fast fault detection, demonstrating robust performance under noisy conditions and topological uncertainties. Building on that foundation, the proposed method utilises current waveform entropy to accurately locate HIFs in noisy environments with no limitation on the network variations, type of fault and value of fault impedance. It incorporates a physical model within an iterative procedure to solve the inverse problem. In this approach, the issue of fault location is formulated as an optimisation process aiming to pinpoint the fault location by minimising an appropriate objective function. This function denotes the disparity between the entropy of the measured current waveforms and their model-predicted counterparts. This paper adopts a hybrid conjugate gradient (HCG) optimisation technique in the inversion process, which is preferred to its stochastic rivals with intrinsic time-consuming searching mechanisms and slow convergence speed [28]. The HCG optimisation technique in this paper includes the standard steepest descent (SSD) and the conjugate gradient (CG) methods; the former exhibits a robust convergence, whereas the latter provides a high convergence speed [29]. Therefore, the main contributions of this paper can be expressed as follows:

- Utilising current waveform entropy to ensure accurate performance under noisy conditions.
- Applying HCG method for fast and robust fault location.
- Accurate fault location in the case of HIFs up to 100 Ω, even under heavy noise conditions with signal-to-noise ratio of 20 dB.

The structure of the rest of this paper is as follows. In Section 2, the concept of *Shannon* entropy is briefly described as a tool for measuring the uncertainty or 'information' of the current waveform. In Section 3, the inversion technique, including the derivation of the objective function and the implementation of the HCG method, is explained. In Section 4, the results of several case studies are presented to evaluate the efficacy of the proposed method when applying to a typical mesh-type DC microgrid. Finally, in Section 5, the comparison between the proposed technique and the state-of-the-art fault location methods is presented.

2 | Entropy of Varying Current Waveform

Consider the DC system shown in Figure 1 where a ring DC microgrid is connected to various DC sources/loads (via DC/DC links) and AC sources/loads (via DC/AC links). The system is protected by appropriate protective relay that can measure the respective line currents. Assume that the lth line experiences a pole-to pole (PP) fault at point F1 or a pole-to-ground (PG) fault at point F2 that was already detected by the respective relay. In the proposed scheme, the variations of entropy of the current waveforms are utilised to determine the location of the fault.

A brief account of *Shannon* entropy is first provided, followed by an explanation of how it can be used to derive the entropy of a varying current waveform.

2.1 | Shannon Entropy

Shannon entropy is a measure to quantify the mean value of information in a signal [30, 31]. Consider X as a discrete random variable, characterised by a cardinality of $N(X = [x_1 : x_N])$ and probability mass function $P(x_n)$; $n = 1, \ldots, N$. The entropy of X, defined as a non-negative quantity $H(X)$, can be expressed as follows [25]:

$$H(X) = -\sum_{n=1}^{N} P(x_n)\log_2 P(x_n), \tag{1}$$

where $0 \times \log 0 = 0, 0 \leq P(x_n) \leq 1$ and $\sum\limits_{n=1}^{N} P(x_n) = 1$.

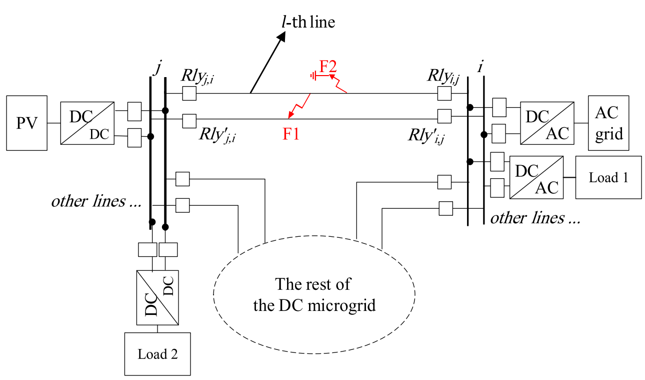

FIGURE 1 | An example of a ring DC microgrid experiencing a PP fault (F1) or a PG fault (F2) on the lth line.

Using Equation (1), the entropy of a sampled current signal, $\mathbf{I} = [I_1; I_2 \ldots I_N]$, can be determined as follows [27]:

$$SE(\mathbf{I}) = -\sum_{n=1}^{N} I_n^{\mathrm{norm}} \log_2\left(I_n^{\mathrm{norm}}\right), \tag{2a}$$

where I_n^{norm} is the normalised value of I_n, that is,

$$I_n^{\mathrm{norm}} = \frac{\mathbf{I} - \min(\mathbf{I}) + \varepsilon}{\sum_{n=1}^{N} [I_n - \min(\mathbf{I}) + \varepsilon]}. \tag{2b}$$

Here, ε represents a small positive figure to avoid mathematical ambiguity.

2.2 | Fault Response

When a fault occurs, the current waveform undergoes rapid changes, forming a random signal.

Referring to Equation (2), the variation in the current signal entropy, measured by a protective relay Rly, $\Delta SE_{\mathrm{I}}(Rly)$, stationed at the two ends of the faulty line can be expressed as follows [27]:

$$\Delta SE_{\mathrm{I}}(Rly) = \log_2 N - SE_{\mathrm{I}}(Rly). \tag{3}$$

In the normal condition, $SE_{\mathrm{I}}(Rly)$ has its maximum value, $\log N$, indicating that the value of $\Delta SE_{\mathrm{I}}(Rly)$ is zero. During a fault event, the current magnitude rapidly increases, causing the respective value of ΔSE_{I} to increase. Assuming a discretised current signal in an N-sample running window, where N_1 samples precede and N_2 samples follow the fault occurrence, Equations (2) and (3) lead to the following:

$$\Delta SE_{\mathrm{I}}(Rly) = \log_2 N + \sum_{n_1=1}^{N_1} i_{n_1}^{\mathrm{norm}} \log_2\left(i_{n_1}^{\mathrm{norm}}\right) + \sum_{n_2=(N_1+1)}^{N} i_{n_2}^{\mathrm{norm}} \log_2\left(i_{n_2}^{\mathrm{norm}}\right),$$

where $N = N_1 + N_2$.

To predict the fault current, this paper adopts the model used in Bayati et al. [20]. In this model, when a fault occurs, the DC link capacitors at both ends of the faulty line (say connecting bus-i and bus-j) start to discharge and contribute to the fault current as shown in Figure 2 [20]. Referring to this figure, the fault current injected from bus-j can be expressed as follows [20]:

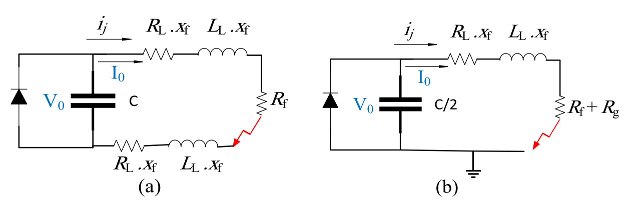

FIGURE 2 | Equivalent circuit during DC link capacitor discharge; (a) PP fault and (b) PG fault.

$$i_j(t) = e^{-\alpha t}\left(\frac{V_0}{\omega x_{\mathrm{f}} L_{\mathrm{L}}}\sin(\omega t) - \frac{I_0\omega_0}{\omega}\sin(\omega t + \beta)\right), \tag{4}$$

where V_0 and I_0 are, respectively, the capacitor link voltage and injected current from bus-j just before the occurrence of the fault, $\omega = \sqrt{{\omega_0}^2 - \alpha^2}$, and $\beta = \tan^{-1}\frac{\omega}{\alpha}$. Also, in the case of a PP fault (Figure 2a) $\alpha = \frac{R_{\mathrm{L}}x_{\mathrm{f}} + 0.5R_{\mathrm{f}}}{2x_{\mathrm{f}}L_{\mathrm{L}}}$ and $\omega_0 = \frac{1}{\sqrt{2L_{\mathrm{L}}x_{\mathrm{f}}C}}$, whereas when a PG fault (Figure 2b) occurs $\alpha = \frac{R_{\mathrm{L}}x_{\mathrm{f}} + R_{\mathrm{f}} + R_{\mathrm{g}}}{2x_{\mathrm{f}}L_{\mathrm{L}}}$ and $\omega_0 = \frac{2}{\sqrt{L_{\mathrm{L}}x_{\mathrm{f}}C}}$. Here, R_{L} and L_{L} represent the line resistance and inductance, respectively, while x_{f} and R_{f} denote the fault location and fault resistance, respectively.

Similar expressions can be derived for the discharging fault current due to the DC link capacitors at bus-i, contributing to the PP and PG fault currents.

3 | Determination of Fault Location

The goal is to determine the fault location (Figure 1) from the entropy variation of the current waveform, measured at the two ends of the faulty line. To achieve this, first, an initial value is assumed for the unknown variable $(x_{\mathrm{f}}, R_{\mathrm{f}})$. Then, for the given values of x_{f} and R_{f} an objective function is calculated based on the difference between the measured and estimated values of the current signal entropy, $\Delta SE_{\mathrm{I}}(Rly)$, by a protective relay Rly stationed at the two ends of the faulty line. Finally, the determination of unknown variables is achieved by employing the HCG method, which seeks to minimise the objective function in an iterative process.

3.1 | Objective Function

Referring to Figure 1, the objective function, $OF(\boldsymbol{x})$, and its gradient, $g(\boldsymbol{x})$ for the ith side of the faulty line can be stated as follows:

$$OF(\boldsymbol{x}) = \left(\Delta SE_{\mathrm{I}}^{\mathrm{p}}(Rly_{i,j}) - \Delta SE_{\mathrm{I}}^{\mathrm{m}}(Rly_{i,j})\right)^2, \tag{5a}$$

$$\begin{aligned} g_{x_n}(\boldsymbol{x}) &= \nabla_{x_n}(OF(\boldsymbol{x})) \\ &= 2\left(\Delta SE_{\mathrm{I}}^{\mathrm{p}}(Rly_{i,j}) - \Delta SE_{\mathrm{I}}^{\mathrm{m}}(Rly_{i,j})\right)\nabla_{x_n}\left(\Delta SE_{\mathrm{I}}^{\mathrm{p}}(Rly_{i,j})\right) \end{aligned}, \tag{5b}$$

where $\boldsymbol{x}^{\mathrm{T}} = (x_f, R_f)$, $n = 1, 2$, $\Delta SE_{\mathrm{I}}^{\mathrm{p}}(Rly_{i,j})$ and $\Delta SE_{\mathrm{I}}^{\mathrm{m}}(Rly_{i,j})$ are, respectively, the predicted and measured values of the changes in the current signal entropy corresponding to the protection unit at the ith bus (Figure 1). Similar expressions can be derived for the jth side of the faulty line by changing $Rly_{i,j}$ with $Rly_{j,i}$.

Provided that the values of current signal entropy, computed by the protective relays at both ends of the faulty line are accessible through communication links, the objective function, $OF(\boldsymbol{x})$, and its gradient, $g(\boldsymbol{x})$ can be stated as follows:

$$\begin{aligned} OF(\boldsymbol{x}) &= \left(\Delta SE_{\mathrm{I}}^{\mathrm{p}}(Rly_{i,j}) - \Delta SE_{\mathrm{I}}^{\mathrm{m}}(Rly_{i,j})\right)^2 \\ &\quad + \left(\Delta SE_{\mathrm{I}}^{\mathrm{p}}(Rly_{j,i}) - \Delta SE_{\mathrm{I}}^{\mathrm{m}}(Rly_{j,i})\right)^2 \end{aligned}, \tag{6a}$$

$$\begin{aligned} g_{x_n}(\mathbf{x}) &= \nabla_{x_n}(OF(\mathbf{x})) \\ &= 2\left(\Delta SE_{\mathrm{I}}^{\mathrm{p}}(Rly_{i,j}) - \Delta SE_{\mathrm{I}}^{\mathrm{m}}(Rly_{i,j})\right)\nabla_{x_n}\left(\Delta SE_{\mathrm{I}}^{\mathrm{p}}(Rly_{i,j})\right), \\ &\quad + 2\left(\Delta SE_{\mathrm{I}}^{\mathrm{p}}(Rly_{j,i}) - \Delta SE_{\mathrm{I}}^{\mathrm{m}}(Rly_{j,i})\right)\nabla_{x_n}\left(\Delta SE_{\mathrm{I}}^{\mathrm{p}}(Rly_{j,i})\right) \end{aligned} \tag{6b}$$

where $\boldsymbol{x}^{\mathrm{T}} = (x_f, R_f)$, $n = 1, 2$, $\Delta SE_{\mathrm{I}}^{\mathrm{p}}(Rly_{i,j})$ and $\Delta SE_{\mathrm{I}}^{\mathrm{p}}(Rly_{j,i})$ are, respectively, the predicted values of the changes in the current signal entropy corresponding to the protection relays at the both ends of the faulty line at the ith and jth buses (Figure 1), and $\Delta SE_{\mathrm{I}}^{\mathrm{m}}(Rly_{i,j})$ and $\Delta SE_{\mathrm{I}}^{\mathrm{m}}(Rly_{j,i})$ are their respective measured values.

3.2 | Hybrid Conjugate Gradient Method

This paper adopts the HCG scheme for minimising the objective function defined in Equations 5(a) or 6(a). This is done in an iterative process, as shown in Figure 3. It begins with execution of the CG method and updates the unknown parameter values in each iteration. The unknown parameters at the kth iteration, $\boldsymbol{x}_k$, are employed to compute the corresponding value of $OF(\boldsymbol{x}_k)$. The inversion process is completed when the value of $OF(\boldsymbol{x}_k)$ becomes below a pre-specified threshold value, OF_{Th}, in which case the elements of $\boldsymbol{x}_k$ will represent the approximated values of the unknown variables. In other cases, a new value of $OF(\boldsymbol{x}_k)$ is computed by updating $\boldsymbol{x}_k$ in the next iteration as follows [29]:

$$\boldsymbol{x}_{k+1} = \boldsymbol{x}_k + \alpha_k \boldsymbol{d}_k, \tag{7a}$$

where α_k is an adjustable step size that is calculated with the aid of the backtracking-Armijo line search [32]. Also, $\boldsymbol{d}_k$ represents the search direction along which the value of OF decreases:

$$\mathbf{d}_k = -\mathbf{g}_k + \beta_k \mathbf{d}_{k-1}. \tag{7b}$$

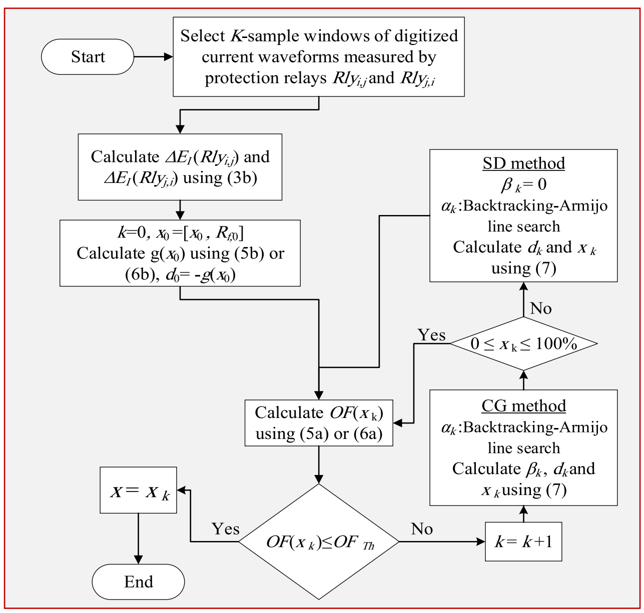

FIGURE 3 | A flowchart of the proposed HCG scheme for determining the fault location.

Here, $\mathbf{g}_k^T = \left(g_{x_{1,k}}, g_{x_{2,k}}\right)$ whose elements can be computed using Equations 5(b) or 6(b). The hybrid parameter is defined as follows:

$$\beta_k = \begin{cases} \beta_k^{\text{FR}} & 0 \le x_{1,k} \le 100\% \text{ and } 0 \le x_{2,k} \\ 0 & \text{otherwise} \end{cases}, \tag{7c}$$

where $\beta_k^{\text{FR}} = \frac{g_k^T g_k}{g_{k-1}^T g_{k-1}}$ represents the Fletcher–Reeves conjugate gradient coefficient [29] becoming zero when the predicted value of x_k lies outside its permissible range.

In the case where $\beta_k = 0$, the CG method is stopped and the new value of $\boldsymbol{x}_k$ is calculated using the SSD technique. The switching from the CG method to the SSD method almost guarantees the solution of the problem despite its relatively slow convergence. This is because of the fact that the SSD method renews the solution process from the latest value of $\boldsymbol{x}$ which is nearer to the ultimate solution point, not affected by its initial value [29].

4 | Simulation Results

To evaluate the effectiveness of the proposed fault location scheme, the results of various case studies are reported in this section. These studies focus on a 5-bus mesh-type DC microgrid, illustrated in Figure 4 (with data available in Kong and Nian [22]). It integrates distributed generation (DG) resources, including a wind turbine (WT) and photovoltaic (PV) system to serve a DC load. The microgrid is linked to the AC grid using an appropriate DC/AC converter.

The following simulations are conducted in MATLAB-Simulink. A 10 kHz sampling frequency is applied to a sliding window of 100 samples from the digitised current waveform. This approach ensures a sampling period approximately one-10th of the minimum time required for the fault current to reach its peak value at various locations [33]. The parameter settings applied throughout the simulations are summarised in Table 1 to ensure reproducibility and facilitate future research.

It is assumed that the fault occurs at $t = 1$ s and is detected at 0.1 ms after its occurrence. Upon detection, the digitised current waveforms recorded in the sliding windows of the respective protection relays at the time of the fault are input to the fault location algorithm (Figure 3).

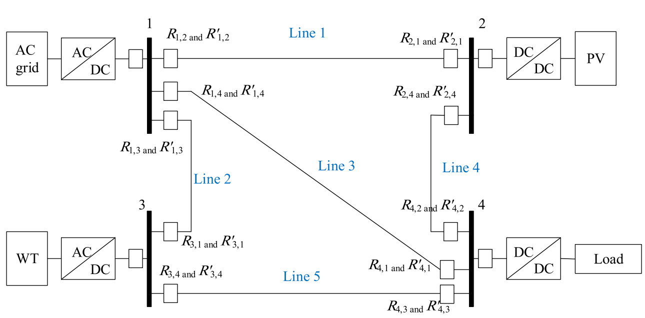

FIGURE 4 | Single-line schematic diagram of the sample mesh-type DC microgrid [22].

In all case studies, the predicted results are compared with those derived using one of the recent advanced fault location techniques applicable to DC microgrids [22]. In Kong and Nian [22], the Pearson correlation coefficient is used to measure a linear correlation between the fault location and the fault current waveform observed by the respective protection relays. Also, the genetic algorithm (GA) is adopted to update the estimated location scheme until the correlation coefficient becomes higher than a pre-specified threshold. It should be noted that the method [22] utilises only single-ended data. To ensure a fair comparison, results from Kong and Nian [22] are presented using both single-ended and double-ended data.

4.1 | Validity

For demonstration purposes, the validity of the proposed method is analysed under various fault conditions on lines 1 and 2 of the microgrid in Figure 4. Specifically, a PG fault on 20%, 40%, 60% and 80% of line 2 and a PP fault on 20%, 40%, 60% and 80% of line 1 are simulated. The fault resistance in all cases is considered 1mΩ and the signal-to-noise ratio (SNR) is assumed as 40 dB. The current waveforms observed by the protection relays are plotted in Figure 5a–d for the PG faults at 20%, 40%, 60% and 80% of line 2, respectively. The corresponding values of ΔSE_{I} at the time of fault detection for these PG faults are plotted in Figure 6a–d, respectively. Similar curves for the PP faults are plotted in Figures 7a–d and 8a–d. An examination of the results in these figures denotes that the value of ΔSE_{I} tends to increase as the fault approaches the respective measurement station where a relatively larger fault current is observed.

Next, the accuracy of the proposed method is evaluated in comparison to its rival in Kong and Nian [22]. Assuming $O_{\text{Th}} = 10^{-6}$ as the convergence criterion for both methods, the fault location errors associated with PG and PP faults are given in Tables 2 and 3, respectively. An examination of the results in these tables denotes that both methods can accurately locate the

TABLE 1 | Simulation parameter settings.

Parameter	Value/description
Sampling frequency	10 kHz
Window size	10 ms
Convergence threshold	10^{-6}
Fault resistance range	1 mΩ–100 Ω
Fault initiation time	1 s
HCG starting point	$\left(x_{\text{f}}, R_{\text{f}}\right) = (50\%, 0.01\ \Omega)$
Simulation platform	MATLAB/Simulink
Noise model/signal-to-noise ratio	Additive white Gaussian noise (AWGN)/40 and 20 dB
Fault type	PG and PP
Simulation duration/step size	1.2 s/1 µs

fault in all cases. However, the proposed method yields a more accurate location of a fault as compared to its rival. This is correct in all cases, using the data measured at one side or two sides of the faulty line. A further study of the results shows that the accuracy of the proposed method improves when the measured values of $\Delta SE_I(Rly)$ at two sides of the faulty lines are available through a communication link.

Finally, each line is subjected to the same fault scenarios. Tables 4 and 5 compare PG fault location errors using the measured data from one end and both ends of the lines, respectively, and Tables 6 and 7 provide the same comparison for PP faults. The results clearly demonstrate the improved accuracy of the proposed method compared to the method in Kong and Nian [22].

4.2 | Computation Efficiency

To evaluate computational efficiency, the computation times for all case studies are obtained. Tables 8–11 present the CPU times obtained using an Intel Core i7-5500U processor at 2.4 GHz with 8 GB of RAM running MATLAB software. These results demonstrate that the proposed scheme is significantly faster than the method in Kong and Nian [22], particularly when using data from only one side of the faulty line for fault location (approximately 27 times faster on average with a maximum speed improvement of up to 75 times).

The use of the HCG method plays an important role in the computation efficiency of the proposed method. This is demonstrated in the results provided in Table 12 where the

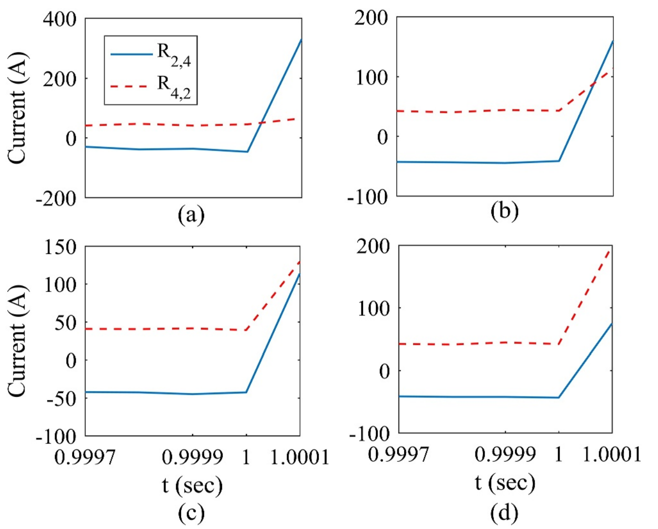

FIGURE 5 | Varying current magnitude observed by the relays at both ends of the faulty line during a PG fault at $t = 1$ s on (a) 20%, (b) 40% (c), 60% and (d) 80% of line 2 shown in Figure 4.

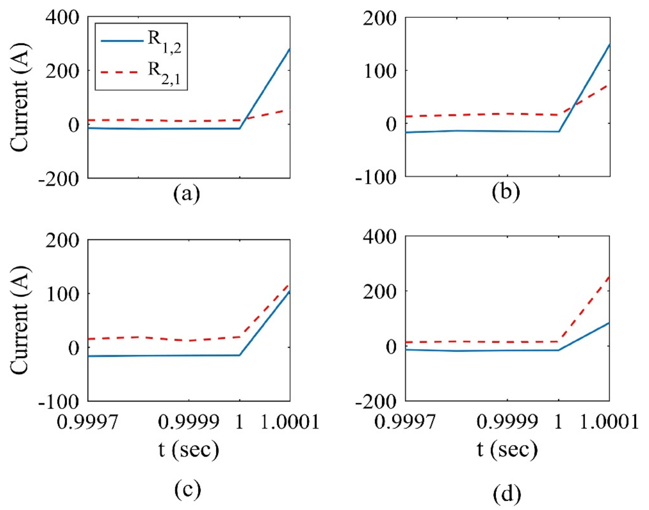

FIGURE 7 | Varying current magnitude observed by the relays at both ends of the faulty line during a PP fault at $t = 1$ s on (a) 20%, (b) 40%, (c) 60% and (d) 80% of line 1 shown in Figure 4.

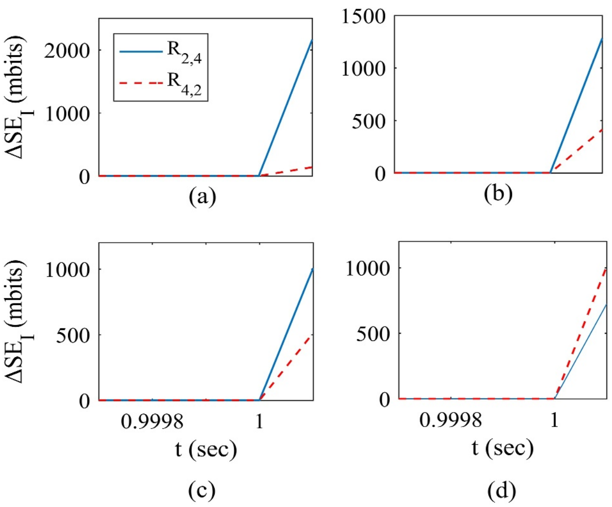

FIGURE 6 | Values of ΔSE_I corresponding to the varying current magnitude (Figure 5) observed by the relays at both ends of the faulty line during a PG fault at $t = 1$ s on (a) 20%, (b) 40%, (c) 60% and (d) 80% of line 2 shown in Figure 4.

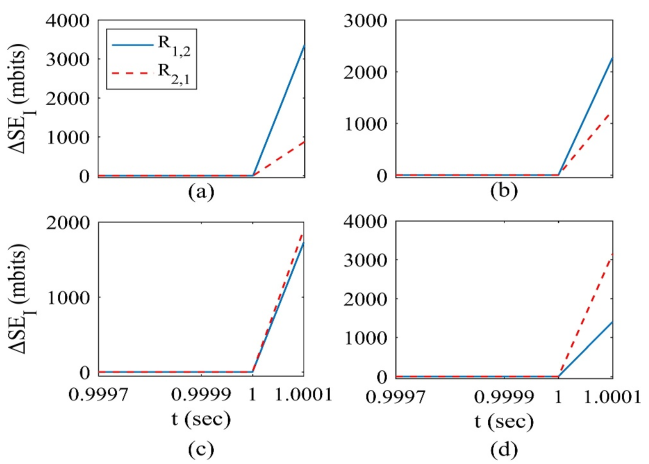

FIGURE 8 | Values of ΔSE_I corresponding to the varying current magnitude (Figure 7) observed by the relays at both ends of the faulty line during a PP fault at $t = 1$ s on (a) 20%, (b) 40%, (c) 60% and (d) 80% of line 1 shown in Figure 4.

TABLE 2 | Fault location errors (%) in the case of a PG fault occurring at line 2 in the microgrid shown in Figure 4.

Method		Fault location along the faulty line (percentage of line length)			
		20	40	60	80
Proposed scheme	One end	0.71	0.64	0.78	0.78
Kong and Nian [22]	One end	0.89	1.44	1.05	1.14
Proposed scheme	Both ends	0.27	0.40	0.28	0.47
Kong and Nian [22]	Both ends	0.63	0.81	0.62	0.74

TABLE 3 | Fault location errors (%) in the case of a PP fault occurring at line 1 in the microgrid shown in Figure 4.

Method		Fault location along the faulty line (percentage of line length)			
		20	40	60	80
Proposed scheme	One end	1.16	1.22	0.61	1.58
Kong and Nian [22]	One end	1.21	1.53	1.18	1.64
Proposed scheme	Both ends	0.13	0.18	0.28	0.71
Kong and Nian [22]	Both ends	0.75	0.68	0.73	0.82

HCG method is compared with the CG [28] and SSD [32] methods in the case of a PG fault with a resistance of 50 Ω at 50% of each line. The objective function for all methods is considered as Equation (6a), and 20 dB noise is considered in all scenarios. As shown in Table 12, the HCG method shows a better performance compared to the other methods. The CG method failed to converge in most scenarios. This is because this method is very fast and used for optimisation in a non-limited variables. Therefore, in a few iterations, the estimated values of fault location and its resistance exceed their boundaries and causing the algorithm to diverge. On the other hands, the SSD method can accurately locate faults in all cases but has slower convergence, taking about 5.9 times longer than the proposed method.

4.3 | High Impedance Faults

To analyse the impact of fault resistance on the performance of the proposed method, a PG fault is simulated at 50% of line 3 (Figure 4) with fault resistances of 10, 50 and 100 Ω, and an SNR of 20 dB. The current waveforms observed by the protective relays at both ends of the faulty line at the time of fault detection are captured and these data are used to compute the corresponding ΔSE_{I} values (Figures 9 and 10). The current waveforms observed by the protection relays are plotted in

TABLE 4 | Fault location errors (%) for PG faults in the microgrid of Figure 4 using the measured data from one end of the lines.

Faulty line number	Fault location along the faulty line (percentage of line length)							
	20		40		60		80	
	Proposed scheme	Kong and Nian [22]	Proposed scheme	Kong and Nian [22]	Proposed scheme	Kong and Nian [22]	Proposed scheme	Kong and Nian [22]
1	0.62	0.73	0.7	0.88	0.99	1.18	0.94	1.05
2	0.71	0.89	0.64	1.44	0.78	1.05	0.78	1.14
3	0.89	1.22	1.72	1.9	0.74	1.82	0.58	1.21
4	0.47	0.61	0.81	1.01	0.84	0.94	1.02	1.93
5	0.51	0.64	1.14	1.56	0.97	1.07	1.15	1.34
Ave. error	0.64	0.82	1	1.36	0.86	1.21	0.89	1.33

TABLE 5 | Fault location errors (%) for PG faults in the microgrid of Figure 4 using the measured data from two ends of the lines.

Faulty line number	Fault location along the faulty line (percentage of line length)							
	20		40		60		80	
	Proposed scheme	Kong and Nian [22]	Proposed scheme	Kong and Nian [22]	Proposed scheme	Kong and Nian [22]	Proposed scheme	Kong and Nian [22]
1	0.31	0.66	0.38	0.75	0.47	0.82	0.27	0.74
2	0.27	0.63	0.40	0.81	0.28	0.62	0.47	0.74
3	0.31	0.74	0.56	0.89	0.41	0.95	0.62	0.85
4	0.23	0.58	0.43	0.92	0.45	0.79	0.31	1.01
5	0.35	0.52	0.47	0.86	0.37	0.68	0.67	0.83
Ave. error (%)	0.29	0.63	0.45	0.85	0.4	0.77	0.47	0.83

TABLE 6 | Fault location errors (%) for PP faults in the microgrid of Figure 4 using the measured data from one end of the lines.

Faulty line number	Fault location along the faulty line (percentage of line length)							
	20		40		60		80	
	Proposed scheme	Kong and Nian [22]	Proposed scheme	Kong and Nian [22]	Proposed scheme	Kong and Nian [22]	Proposed scheme	Kong and Nian [22]
1	1.16	1.21	1.22	1.53	0.61	1.18	1.58	1.64
2	0.77	1.08	0.86	0.93	0.98	1.36	0.71	0.89
3	0.66	0.73	0.62	0.83	0.84	0.98	0.94	1.13
4	1.05	1.08	0.47	0.62	0.73	1.77	1.01	1.42
5	0.85	0.96	1.07	1.58	1.09	1.35	0.79	1.41
Ave. error (%)	0.9	1.01	0.85	1.1	0.85	1.33	1.01	1.3

TABLE 7 | Fault location errors (%) for PP faults in the microgrid of Figure 4 using the measured data from both ends of the lines.

Faulty line number	Fault location along the faulty line (percentage of line length)							
	20		40		60		80	
	Proposed scheme	Kong and Nian [22]	Proposed scheme	Kong and Nian [22]	Proposed scheme	Kong and Nian [22]	Proposed scheme	Kong and Nian [22]
1	0.13	0.75	0.18	0.68	0.28	0.73	0.71	0.82
2	0.19	0.88	0.47	0.73	0.68	0.8	0.52	0.66
3	0.08	0.72	0.31	0.77	0.48	0.74	0.36	0.58
4	0.11	0.65	0.27	0.75	0.46	0.89	0.44	0.88
5	0.22	0.84	0.68	0.94	0.39	0.75	0.57	0.85
Ave. error (%)	0.15	0.77	0.38	0.77	0.46	0.78	0.52	0.76

TABLE 8 | Computational times (second) associated with the results given in Table 4.

Faulty line number	Fault location along the faulty line (percentage of line length)							
	20		40		60		80	
	Proposed scheme	Kong and Nian [22]	Proposed scheme	Kong and Nian [22]	Proposed scheme	Kong and Nian [22]	Proposed scheme	Kong and Nian [22]
1	0.16	2.13	0.15	3.09	0.15	3.87	0.17	5.4
2	0.18	2.26	0.16	2.85	0.16	4.24	0.16	5.07
3	0.16	2.57	0.18	8.96	0.17	3.13	0.15	4.81
4	0.18	2.65	0.16	6.29	0.16	2.97	0.15	11.01
5	0.15	3.96	0.15	1.95	0.17	4.18	0.17	2.65
Ave. time	0.17	2.71	0.16	4.63	0.16	3.68	0.16	5.79

Figure 9a–c for the PG faults with resistances of 10, 50 and 100 Ω, respectively.

The corresponding values of ΔSE_{I} at the time of fault detection for these PG faults are plotted in Figure 10a–c, respectively. These ΔSE_{I} values are then used to determine the fault location.

Using the same convergence criterion ($O_{\mathrm{Th}} = 10^{-6}$), Table 13 presents the location errors for the proposed method and the method in Kong and Nian [22] under these varying fault resistances. The results demonstrate the high accuracy of the proposed method, especially when utilising current measurements from both ends of the line. In contrast, the method in Kong and Nian [22], when using data only from one side, only achieves accuracy for a 10 Ω fault resistance and fails to converge for a 50 Ω fault. Although [22], can locate a fault with 50 Ω resistance when using current measurements from both ends of the line, it fails to converge for a 100 Ω fault.

The same scenario is applied to each line in the microgrid (Figure 4) to assess the performance of the proposed method under varying line conditions. Tables 14 and 15 present the fault location errors when using the measured data from one end and both ends of the lines, respectively. As these results demonstrate, the proposed method offers improved accuracy compared to the method in Kong and Nian [22], particularly when

TABLE 9 | Computational times (second) associated with the results given in Table 5.

	Fault location along the faulty line (percentage of line length)							
	20		40		60		80	
Faulty line number	**Proposed scheme**	**Kong and Nian [22]**	**Proposed scheme**	**Kong and Nian [22]**	**Proposed scheme**	**Kong and Nian [22]**	**Proposed scheme**	**Kong and Nian [22]**
1	0.33	4.28	0.32	5.71	0.33	13.68	0.34	6.11
2	0.26	7.03	0.35	6.17	0.34	5.09	0.32	7.84
3	0.24	5.16	0.37	9.14	0.3	4.89	0.31	6.09
4	0.30	4.89	0.34	10.16	0.33	7.22	0.34	9.47
5	0.29	6.33	0.34	6.25	0.28	6.53	0.25	10.08
Ave. time	0.28	5.54	0.34	7.49	0.32	7.48	0.31	7.92

TABLE 10 | Computational times (second) associated with the results given in Table 6.

	Fault location along the faulty line (percentage of line length)							
	20		40		60		80	
Faulty line number	**Proposed scheme**	**Kong and Nian [22]**	**Proposed scheme**	**Kong and Nian [22]**	**Proposed scheme**	**Kong and Nian [22]**	**Proposed scheme**	**Kong and Nian [22]**
1	0.15	4.83	0.14	2.24	0.13	3.5	0.16	11.49
2	0.16	1.57	0.15	3.74	0.17	6.37	0.17	5.18
3	0.17	3.98	0.16	4.37	0.17	2.78	0.16	2.61
4	0.14	2.44	0.14	5.05	0.16	12.08	0.17	2.57
5	0.18	2.65	0.16	1.85	0.15	4.74	0.21	5.66
Ave. time	0.16	3.09	0.15	3.45	0.16	5.9	0.17	5.5

TABLE 11 | Computational times (second) associated with the results given in Table 7.

	Fault location along the faulty line (percentage of line length)							
	20		40		60		80	
Faulty line number	**Proposed scheme**	**Kong and Nian [22]**	**Proposed scheme**	**Kong and Nian [22]**	**Proposed scheme**	**Kong and Nian [22]**	**Proposed scheme**	**Kong and Nian [22]**
1	0.32	6.17	0.23	5.98	0.34	11.92	0.25	14.35
2	0.24	7.25	0.28	9.11	0.33	5.37	0.24	7.21
3	0.28	7.11	0.29	7.68	0.24	7.05	0.25	5.09
4	0.29	5.02	0.29	6.15	0.23	7.63	0.28	5.28
5	0.34	6.4	0.32	7.33	0.26	8.29	0.34	7.92
Ave. time	0.29	6.39	0.28	7.25	0.28	8.05	0.27	7.97

TABLE 12 | Comparison of the performance of HCG, CG [27], SSD [31] and GA for occurrence of a PG fault with resistance of 50 Ω at 50% of each line.

Method	**Average fault location error (%)**	**Average computational times (second)**
CG [28]	NC	—
SSD [32]	1.85	2.71
Proposed HCG	1.85	0.46

Abbreviation: NC, not converged.

utilising data from both ends of the faulty line. Analysis of Tables 14 and 15 reveals that the proposed method achieves fault location errors of ≤ 4.16% in all cases using double-ended line data. With single-ended data, however, fault location errors increase to approximately 10% when the fault resistance reaches 100 Ω. Notably, the method in Kong and Nian [22] struggled to accurately locate faults with resistances exceeding 10 Ω, resulting in errors beyond permissible limits or algorithm convergence failure. Although the authors in Ref. [22] achieved fault location errors of ≤ 7.8% with double-ended data and a fault resistance of 50 Ω, they failed to locate faults with a resistance of 100 Ω.

5 | Discussions

The performance of the proposed fault location method is validated by the case studies presented in the previous sections. To provide a comparative analysis, Table 16 outlines the key features of recent fault location approaches for DC microgrids. It is important to emphasise that this table compiles feature information from published studies rather than simulated data.

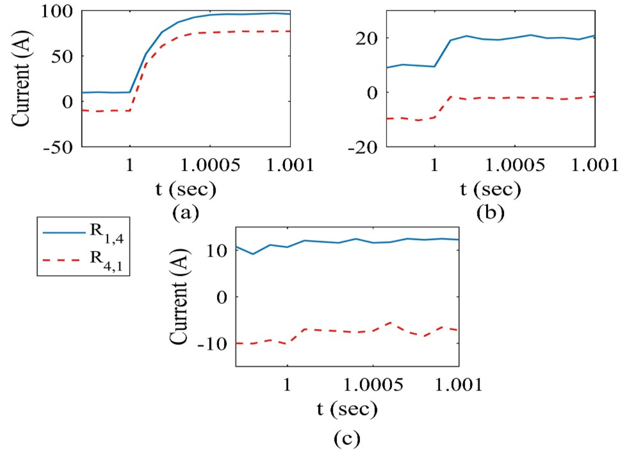

FIGURE 9 | Variations of the current waveforms observed by the relays at both ends of the faulty line when a PG fault at $t = 1$ s with (a) 10 Ω, (b) 50 Ω and (c) 100 Ω resistance occurred in the middle of line 3 shown in Figure 4.

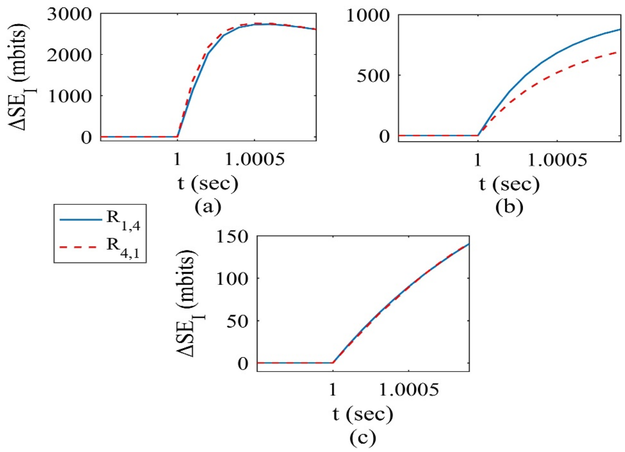

FIGURE 10 | Values of ΔSE_I corresponding to the current waveforms observed by the relays at both ends of the faulty line (Figure 9) when a PG fault at $t = 1$ s with (a) 10 Ω, (b) 50 Ω and (c) 100 Ω resistance occurred in the middle of line 3 shown in Figure 4.

Based on the data in Table 16, it can be inferred that the proposed scheme can accurately locate HIFs with fault resistance as high as 100 Ω and SNR as low as 20 dB. These features outperform the existing methods that cannot function successfully in the presence of noise [21–24] or when the value of SNR is lower than 34 dB [20, 34], not being able to locate HIFs with fault resistance > 20 Ω. Furthermore, unlike [24, 26], the proposed method does not require any additional devices.

The success of the proposed scheme stems from the efficacy of *Shannon* entropy in noisy environments that excels in quantifying the information content of signals, even amidst uncertainty and distortion caused by noise [31, 35]. Besides, the use of an efficient physical model into an iterative approach for resolving the inverse problem has further improved the accuracy and computation efficiency of the proposed method. In fact, the HCG optimisation algorithm in the inversion process has guaranteed the robust and fast convergence of the proposed method [29]. Although the proposed entropy-based inversion method demonstrates high accuracy in locating HIFs under noisy conditions, it has certain limitations that should be acknowledged. Although the method performs well at SNR as low as 20 dB and fault resistances up to 100 Ω, its accuracy may degrade under extreme noise levels below this threshold and fault resistances exceeding 100 Ω. Furthermore, despite the improved convergence speed of the HCG optimisation technique, the iterative nature of the method requires high computational effort that may limit real-time implementation in systems with constrained processing capabilities.

6 | Conclusion

This paper proposes a novel inversion method based on *Shannon* entropy to accurately locate short-circuit faults in DC microgrids. The proposed method adopts a phenomenological approach that uses a physical model to iteratively solve the inverse problem. The problem is posed as an optimisation problem that determines the most likely location of a fault by minimising an appropriate objective function; it represents the disparity between the entropy of the current waveforms observed by the protection relays at the time of fault detection and their model-predicted counterparts. A hybrid conjugate gradient-based approach is adopted to minimise the value of the objective function. It includes the

TABLE 13 | Fault location errors for a PG fault at the middle of line 3 in Figure 4.

Fault resistance (Ω)											
10				50				100			
Proposed scheme		Kong and Nian [22]		Proposed scheme		Kong and Nian [22]		Proposed scheme		Kong and Nian [22]	
One end	Both ends	One end	Both ends	One end	Both ends	One end	Both ends	One end	Both ends	One end	Both ends
2.05	0.39	3.06	3.11	5.03	1.82	NC	7.53	9.06	2.39	18.3	NC

Abbreviation: NC, not converged.

TABLE 14 | Fault location errors (%) for a PG fault at the middle of the lines in the microgrid shown in Figure 4 using the measured data from one end of the lines.

	Fault resistance (Ω)					
	10		**50**		**100**	
Faulty line number	**Proposed scheme**	**Kong and Nian [22]**	**Proposed scheme**	**Kong and Nian [22]**	**Proposed scheme**	**Kong and Nian [22]**
1	2.73	5.85	4.98	9.16	8.43	NC
2	1.79	3.80	4.22	8.29	8.02	11.38
3	2.05	3.06	5.03	NC	9.06	18.3
4	3.02	5.01	4.38	10.52	9.82	NC
5	2.61	4.19	4.31	9.43	9.11	17.91
Ave. error	2.44	4.38	4.58	NC	8.89	NC

Abbreviation: NC, not converged.

TABLE 15 | Fault location errors (%) for a PG fault at the middle of the lines in the microgrid shown in Figure 4 using the measured data from two ends of the lines.

	Fault resistance (Ω)					
	10		**50**		**100**	
Faulty line number	**Proposed scheme**	**Kong and Nian [22]**	**Proposed scheme**	**Kong and Nian [22]**	**Proposed scheme**	**Kong and Nian [22]**
1	0.76	2.85	2.13	6.38	3.46	12.08
2	0.74	3.04	1.18	6.71	2.27	16.63
3	0.39	3.11	1.82	7.53	2.39	NC
4	0.98	3.7	2.12	7.02	4.16	18.05
5	0.93	3.62	1.98	7.8	2.73	13.29
Ave. error	0.76	3.26	1.85	7.09	3	NC

Abbreviation: NC, not converged.

TABLE 16 | Comparison of the proposed method with recent fault location schemes.

Method	**Maximum error (%)**	**Maximum value of fault resistance (Ω)**	**Signal-to-noise ratio (dB)**	**Need of additional devices**
[22]	4	10	—	No
[21]	6	6	—	No
[24]	5	50	—	CLR, SGR
[23]	4.7	200	—	No
[26]	7.3	200	10	CLR, noise filter
[34]	1.7	1	40	No
[20]	5	20	34	No
Proposed method	4.2	100	20	No

standard steepest descent method for its robust convergence and the conjugate gradient method for its high convergence speed. Simulations have been conducted on a mesh-type DC microgrid to verify the performance of proposed method. The results show that the proposed technique is significantly resilient in the noisy environment and can accurately locate a high impedance fault with fault resistance as high as 100 Ω and signal-to-noise ratio (SNR) as low as 20 dB. In addition, the proposed scheme converges much faster compared to existing methods. These features outperform the existing methods that cannot function successfully in the presence of noise, or when SNR is lower than 34 dB, not being able to locate a high impedance fault with fault resistance > 20 Ω, or needing additional device for increasing their performance.

Author Contributions

Reza Rahmani: conceptualization, data curation, formal analysis, investigation, methodology, resources, software, validation, visualization, writing – original draft. **Seyed Hossein Hesamedin Sadeghi:** conceptualization, methodology, supervision, visualization, writing – review and editing. **Hossein Askarian Abyaneh:** supervision. **Mohammad Javad Emadi**: conceptualization.

Acknowledgements

The authors have nothing to report.

Conflicts of Interest

The authors declare no conflicts of interest.

Data Availability Statement

The data that support the findings of this study are available from the corresponding author upon reasonable request.

References

1. N. Bayati, H. R. Baghaee, M. Savaghebi, A. Hajizadeh, M. Soltani, and Z. Lin, "EMD/HT-Based Local Fault Detection in DC Microgrid Clusters," *IET Smart Grid* 5, no. 3 (February 2022): 177–188, https://doi.org/10.1049/stg2.12060.

2. S. A. Hosseini, B. Taheri, S. H. H. Sadeghi, and A. Nasiri, "An Overview of DC Microgrid Protection Schemes and the Factors Involved," *Electric Power Components and Systems* (September 2023): 1–31, https://doi.org/10.1080/15325008.2023.2251469.

3. V. R. K. Aluri and S. R. Samantaray, "An Improved Probe Power Unit (PPU)-Based Fault Location Estimation in Low-Voltage DC Microgrids," *IEEE Transactions on Smart Grid* 15, no. 6 (November 2024): 5514–5525, https://doi.org/10.1109/tsg.2024.3412591.

4. D. Tzelepis, G. Fusiek, A. Dysko, P. Niewczas, C. Booth, and X. Dong, "Novel Fault Location in MTDC Grids With Non-Homogeneous Transmission Lines Utilizing Distributed Current Sensing Technology," *IEEE Transactions on Smart Grid* 9, no. 5 (September 2018): 5432–5443, https://doi.org/10.1109/tsg.2017.2764025.

5. O. M. K. K. Nanayakkara, A. D. Rajapakse, and R. Wachal, "Traveling-Wave-Based Line Fault Location in Star-Connected Multiterminal HVDC Systems," *IEEE Transactions on Power Delivery* 27, no. 4 (October 2012): 2286–2294, https://doi.org/10.1109/tpwrd.2012.2202405.

6. S. Azizi, M. Sanaye-Pasand, M. Abedini, and A. Hassani, "A Traveling-Wave-Based Methodology for Wide-Area Fault Location in Multiterminal DC Systems," *IEEE Transactions on Power Delivery* 29, no. 6 (December 2014): 2552–2560, https://doi.org/10.1109/tpwrd.2014.2323356.

7. S. Dhar, R. K. Patnaik, and P. K. Dash, "Fault Detection and Location of Photovoltaic Based DC Microgrid Using Differential Protection Strategy," *IEEE Transactions on Smart Grid* 9, no. 5 (September 2018): 4303–4312, https://doi.org/10.1109/tsg.2017.2654267.

8. J. Yang, J. E. Fletcher, and J. O'Reilly, "Short-Circuit and Ground Fault Analyses and Location in VSC-Based DC Network Cables," *IEEE Transactions on Industrial Electronics* 59, no. 10 (October 2012): 3827–3837, https://doi.org/10.1109/tie.2011.2162712.

9. X. Feng, L. Qi, and J. Pan, "A Novel Fault Location Method and Algorithm for DC Distribution Protection," *IEEE Transactions on Industry Applications* 53, no. 3 (May 2017): 1834–1840, https://doi.org/10.1109/tia.2017.2666083.

10. A. Meghwani, S. C. Srivastava, and S. Chakrabarti, "Local Measurement-Based Technique for Estimating Fault Location in Multi-Source DC Microgrids," *IET Generation, Transmission & Distribution* 12, no. 13 (May 2018): 3305–3313, https://doi.org/10.1049/iet-gtd.2017.1801.

11. M. Dashtdar, M. Esmaeilbeig, M. Najafi, and M. E. N. Bushehri, "Fault Location in the Transmission Network Using Artificial Neural Network," *Automatic Control and Computer Sciences* 54, no. 1 (January 2020): 39–51, https://doi.org/10.3103/s0146411620010022.

12. Y. Aslan and Y. E. Yağan, "Artificial Neural-Network-Based Fault Location for Power Distribution Lines Using the Frequency Spectra of Fault Data," *Electrical Engineering* 99, no. 1 (September 2016): 301–311, https://doi.org/10.1007/s00202-016-0428-8.

13. A. C. Adewole, R. Tzoneva, and S. Behardien, "Distribution Network Fault Section Identification and Fault Location Using Wavelet Entropy and Neural Networks," *Applied Soft Computing* 46 (September 2016): 296–306, https://doi.org/10.1016/j.asoc.2016.05.013.

14. M. Gholami, A. Abbaspour, M. Moeini-Aghtaie, M. Fotuhi-Firuzabad, and M. Lehtonen, "Detecting the Location of Short-Circuit Faults in Active Distribution Network Using PMU-Based State Estimation," *IEEE Transactions on Smart Grid* 11, no. 2 (March 2020): 1396–1406, https://doi.org/10.1109/tsg.2019.2937944.

15. L. Li, H. Gao, W. Cong, and T. Yuan, "Location Method of Single Line-to-Ground Faults in Low-Resistance Grounded Distribution Networks Based on Ratio of Zero-Sequence Admittance," *International Journal of Electrical Power & Energy Systems* 146 (March 2023): 108777, https://doi.org/10.1016/j.ijepes.2022.108777.

16. M. Dashtdar, K. Sarada, S. M. S. Hosseinimoghadam, et al., "Faulty Section Identification and Fault Location in Power Network Based on Histogram Analysis of Three-Phase Current and Voltage Modulated," *Journal of Electrical Engineering & Technology* 17, no. 5 (April 2022): 2631–2647, https://doi.org/10.1007/s42835-022-01079-2.

17. A. A. A. Mohd Amiruddin, H. Zabiri, S. A. A. Taqvi, and L. D. Tufa, "Neural Network Applications in Fault Diagnosis and Detection: An Overview of Implementations in Engineering-Related Systems," *Neural Computing & Applications* 32, no. 2 (December 2018): 447–472, https://doi.org/10.1007/s00521-018-3911-5.

18. M. Manohar, E. Koley, and S. Ghosh, "A Reliable Fault Detection and Classification Scheme Based on Wavelet Transform and Ensemble of SVM for Microgrid Protection," in *2017 3rd International Conference on Applied and Theoretical Computing and Communication Technology (iCATccT)* (2017), 24–28, https://doi.org/10.1109/ICATCCT.2017.8389101.

19. S. A. Rocha, T. G. Mattos, R. T. N. Cardoso, and E. G. Silveira, "Applying Artificial Neural Networks and Nonlinear Optimization Techniques to Fault Location in Transmission Lines—Statistical Analysis," *Energies* 15, no. 11 (January 2022): 4095, https://doi.org/10.3390/en15114095.

20. N. Bayati, E. Balouji, H. R. Baghaee, et al., "Locating High-Impedance Faults in DC Microgrid Clusters Using Support Vector Machines," *Applied Energy* 308 (February 2022): 118338, https://doi.org/10.1016/j.apenergy.2021.118338.

21. N. Bayati, H. R. Baghaee, H. Amin, M. Soltani, Z. Lin, and M. Savaghebi, "Local Fault Location in Meshed DC Microgrids Based on Parameter Estimation Technique," *IEEE Systems Journal* 16, no. 1 (March 2022): 1606–1615, https://doi.org/10.1109/jsyst.2021.3107905.

22. L. Kong and H. Nian, "Fault Detection and Location Method for Mesh-Type DC Microgrid Using Pearson Correlation Coefficient," *IEEE Transactions on Power Delivery* 36, no. 3 (2020): 1–1439, https://doi.org/10.1109/tpwrd.2020.3008924.

23. M. H. Ibrahim, E. A. Badran, and M. H. Abdel-Rahman, "Detect, Classify, and Locate Faults in DC Microgrids Based on Support Vector Machines and Bagged Trees in the Machine Learning Approach," *IEEE*

Access 12 (2024): 139199–139224, https://doi.org/10.1109/access.2024.3466652.

24. K. Mahtani, J. M. Guerrero, J. Decroix, and C. A. Platero, "A Simple Single-Ended Post-Fault Location Technique for DC Lines Based on Controlled Re-Energizations," *Electronics* 14, no. 2 (January 2025): 275, https://doi.org/10.3390/electronics14020275.

25. Z. Shuai, L. Wu, L. He, et al., "Fault Location Method Using Local Incipient Current Features for Submarine DC Power Systems," *IEEE Transactions on Instrumentation and Measurement* 74 (January 2025): 1–15, https://doi.org/10.1109/tim.2025.3545717.

26. V. Nougain, S. Mishra, S. S. Nag, and A. Lekić, "Fault Location Algorithm for Multi-Terminal Radial Medium Voltage DC Microgrid," *IEEE Transactions on Power Delivery* 38, no. 6 (September 2023): 4476–4488, https://doi.org/10.1109/tpwrd.2023.3318689.

27. R. Rahmani, S. H. H. Sadeghi, H. Askarian-Abyaneh, and M. J. Emadi, "An Entropy-Based Scheme for Protection of DC Microgrids," *Electric Power Systems Research* 228 (March 2024): 110010, https://doi.org/10.1016/j.epsr.2023.110010.

28. T. Heidari and S. H. H. Sadeghi, "An Efficient Phenomenological Inversion Method for Reconstruction of Crack Depth Profile in a Metal From ACFM Probe Output Signals," *IEEE Open Journal of Instrumentation and Measurement* 1 (January 2022): 1–9, https://doi.org/10.1109/ojim.2022.3205672.

29. M. Shamgholi and S. H. H. Sadeghi, "Simultaneous Measurement of Radius and Coating Thickness of Finite Length Metal Rods by Eddy Current Surface Probes," *IEEE Transactions on Instrumentation and Measurement* 71 (2022): 1–9, https://doi.org/10.1109/tim.2022.3187738.

30. C. E. Shannon, "A Mathematical Theory of Communication," *Bell System Technical Journal* 27, no. 3 (July 1948): 379–423, https://doi.org/10.1002/j.1538-7305.1948.tb01338.x.

31. T. M. Cover and J. A. Thomas, *Elements of Information Theory*. 2nd ed. (John Wiley & Sons, 2006).

32. N. Andrei, *Nonlinear Conjugate Gradient Methods for Unconstrained Optimization* (Springer International Publishing, 2020).

33. A. Meghwani, S. C. Srivastava, and S. Chakrabarti, "A Non-Unit Protection Scheme for DC Microgrid Based on Local Measurements," *IEEE Transactions on Power Delivery* 32, no. 1 (February 2017): 172–181, https://doi.org/10.1109/tpwrd.2016.2555844.

34. P. Chauhan, C. P. Gupta, and M. Tripathy, "High Speed Fault Detection and Localization Scheme for Low Voltage DC Microgrid," *International Journal of Electrical Power & Energy Systems* 146 (March 2023): 108712, https://doi.org/10.1016/j.ijepes.2022.108712.

35. Y. Zhang, Q. Zhang, and S. Wu, "Entropy-Based Robust Spectrum Sensing in Cognitive Radio," *IET Communications* 4, no. 4 (2010): 428–436, https://doi.org/10.1049/iet-com.2009.0389.